Applied Materials Today 11 (2018) 70–81

Contents lists available at ScienceDirect

Applied Materials Today

journal homepage: www.elsevier.com/locate/apmt

MoS_2 and WS_2 nanocone arrays: Impact of surface topography on the hydrogen evolution electrocatalytic activity and mass transport

Daniel Escalera-López[a,b], Ross Griffin[b], Mark Isaacs[c], Karen Wilson[c,d], Richard E. Palmer[e], Neil V. Rees[a,*]

[a] Centre for Hydrogen and Fuel Cell Research, School of Chemical Engineering, University of Birmingham, Birmingham B15 2TT, UK
[b] Nanoscale Physics Research Laboratory, School of Physics and Astronomy, University of Birmingham, Birmingham B15 2TT, UK
[c] European Bioenergy Research Institute, Aston University, Birmingham B4 7ET, UK
[d] School of Science, RMIT University, 124 La Trobe Street, Melbourne, VIC 3000, Australia
[e] College of Engineering, Swansea University, Bay Campus, Fabian Way, Swansea SA1 8EN, UK

ARTICLE INFO

Article history:
Received 1 December 2017
Received in revised form 22 January 2018
Accepted 24 January 2018

Keywords:
Transition metal dichalcogenides
Hydrogen evolution
Nanoelectrode array
Plasma etching

ABSTRACT

We report the fabrication and electrochemical study of edge-abundant transition metal dichalcogenide (TMD) nanocone arrays. Time-dependent etching by sequential use of isotropic O_2 and anisotropic SF_6/C_4F_8 plasmas on nanosphere monolayer-modified TMD crystals results in very high coverage nanocone array structures with tunable aspect ratios and interspacings. Electrochemical characterization of these arrays via the hydrogen evolution reaction (HER), using a low proton concentration electrolyte (2 mM $HClO_4$, 0.1 M $NaClO_4$) to reveal morphology-dependent mass transport features at the proton diffusion-controlled region, show significant changes in electrocatalytic behaviour at both WS_2 and MoS_2: notably onset potential shifts of 100 and 200 mV, and Tafel slope decreases of 50 and 120 mV dec^{-1} respectively. These improvements vary according to the geometry of the arrays and the availability of catalytic edge sites, and thus the observed electrochemical behaviour can be rationalized via kinetic and mass transport effects.

1. Introduction

Transition metal dichalcogenides (TMDs) have generated considerable research interest in recent years as inexpensive, earth-abundant catalysts for hydrogen production [1–3], based on theoretical and experimental evidence of their highly catalytic edge sites [4,5].

Numerous reports have subsequently sought to optimize edge site exposure by the preparation of defect-rich nanostructures [6–9], highly conductive composites [10–12], and by doping the initially inactive S-edge sites [13–16] or the semiconducting basal planes [17,18] with transition metals to enhance their activity to the hydrogen evolution reaction (HER). Another approach to electrocatalytic enhancement is via nanolithography to produce high surface area, reproducible nanopillar/nanocone arrays [19]. Nanoelectrode arrays, previously investigated for their enhanced three dimensional mass transport properties (i.e. convergent diffusion) compared with planar geometries (i.e. linear diffusion, as found in 0D nanostructures such as TMD nanosheets) [20–23], have been fabricated with a nanocone motif to obtain improved photoelectrochemical water splitting [24–27], optoelectronics [28,29], supercapacitors [30,31], memresistors [32], lithium-ion batteries [33–35] and biosensing devices [36–39]. Nanoarrayed structures present, consequently, improved geometrically-normalized current intensities and high surface areas, both properties beneficial for improving the HER activity of TMDs. However, examples of TMD nanoarrays for electrocatalytic applications in the literature are scarce [40,41].

This report focuses on the design and optimization of a methodology to obtain nanopillar/nanocone arrays in TMD materials by plasma etching. In brief, monodisperse nanospheres, ordered on top of TMD surfaces (MoS_2 and WS_2), act as nanolithography masks when exposed to oxygen plasma. Subsequent SF_6/C_4F_8 plasma exposure produces nanocone arrays at the TMD surfaces, with aspect ratios and interspacing tunable by plasma etching conditions. The electrocatalytic enhancement in the HER, the electron transfer kinetics, and the improved mass transport properties arising from the nanoarray geometries, are systematically investigated with electrochemical techniques. For this reason, a low proton concentration electrolyte is deliberately employed to gain insight

* Corresponding author.
E-mail address: n.rees@bham.ac.uk (N.V. Rees).

https://doi.org/10.1016/j.apmt.2018.01.006

into HER mass transport effects arising from the nanoarray topology. Exposure of the metallic 1T phase sites along with changes in the surface composition after plasma etching are monitored by X-ray photoelectron spectroscopy. In addition, modification of the nanocone array morphology upon atmospheric exposure and electrochemical ageing is studied by SEM imaging.

2. Material and methods

2.1. TMD nanoarray fabrication

The fabrication method utilized has been developed within the NPRL group [42–44], and recently used for MoS_2 in Ref. [38] (summarized here, see Section 1 ESI). Briefly, MoS_2 (20×10 mm, SPI Supplies, USA) and WS_2 (defect-free, 99.9995% purity, 2D Semiconductors, USA) crystals were cut into rectangles of approximately 1.5×5 mm using a scalpel blade and then attached to glassy carbon (GC) type 2 stubs (2 mm thickness, 5–7 mm diameter, Alfa Aesar, UK) with carbon tape. 20 μL of a 1:1 (vol. ratio) mixture of a 216 ± 4 nm diameter polystyrene-latex nanosphere (NS) suspension (3000 Series Nanosphere, 1 wt.% in water, Thermo Scientific, UK) with absolute ethanol were transferred to a silicon wafer to form, by self-assembly, a NS monolayer with hexagonal close-packed (HCP) structure. Nanospheres deposition onto the TMD-modified GC substrate was performed by attaching the NS-modified silicon wafer to a custom-built vertical positioner. The positioner was adjusted to immerse the wafer into a water-filled Petri dish (30 s) containing the TMD-modified GC stubs attached to the centre of the dish bottom. Finally, the supernatant was extracted with a syringe to promote NS deposition onto the TMD surface by evaporation. SEM micrographs of the resulting samples were acquired to evaluate the coverage and compactness of the NS HCP arrangement (XL 30 SFEG, 5 kV).

Etching of the NS-modified TMDs was performed in an Oxford Instruments Plasmalab NGP 80 Inductively Coupled Plasma (ICP)/Radio Frequency (RF) etcher. Isotropic oxygen plasma etching for 40 s at 30 standard cubic centimetres per minute (sccm) O_2 flow rate and 100 W RF power was performed as an NS shrinking step. Next, exposure to an anisotropic plasma etching mixture of SF_6 (20 sccm) and C_4F_8 (30 sccm) performed under 200 W ICP and 20 W RF power for variable times (15–60 s) was carried out to obtain nanopillar arrays with variable aspect ratios. Both etching steps were performed under pressures of 15 mTorr and chiller temperatures of 20 °C. SEM micrographs of the freshly etched and electrochemically tested samples were acquired to determine the aspect ratio (nanopillar height/base diameter) and interspacing (nanopillar base-to-base distance) of the individual nanostructures in the array (XL 30 SFEG and JEOL 7100F FEG-SEM, 5 kV, tilt angles from 45° to 85°).

2.2. X-ray photoelectron spectroscopy (XPS)

XPS spectra were recorded using a Kratos Axis His spectrometer fitted with an Al Kα (1486.69 eV) X-ray source and a charge neutralizer (Aston University). All spectra were acquired at pressures below 1×10^{-9} Torr. Peak fitting was performed using CASA XPS version 2.3.18PR1.0, employing Shirley backgrounds and spectral energy corrected to the adventitious C 1s peak at 284.6 eV. W 4f regions were fit using a Doniach-Sunjic modified Gaussian–Lorentz lineshape with a spin–orbit doublet separation of 2.17 eV and peak area ratios of 4:3, whilst S 2p regions were fit with a Gaussian–Lorentz lineshape, employing a 1.2 eV spin–orbit doublet separation and peak area ratios of 2:1.

2.3. Electrochemical characterization

Electrochemical measurements were carried out in a thermostated three-electrode electrochemical cell (23 ± 2 °C) with a PC-controlled PGSTAT128N potentiostat (Metrohm Autolab B.V., Netherlands). The electrodes used were a saturated calomel reference electrode (SCE, BAS Inc, Japan), a bright Pt mesh counter electrode (Alfa Aesar Ltd, UK) and the TMD-modified GC custom-built working electrode (see ESI).

All hydrogen evolution experiments were performed in a 2 mM $HClO_4$ (ACS ≥70%, Sigma–Aldrich), 0.1 M $NaClO_4$ (ACS ≥98%, Sigma–Aldrich) solution using a range of voltage scan rates. The TMD electrodes were preconditioned for HER experiments with 10 cycles between −0.045 and −1.645 V versus SCE at a voltage scan rate of 50 mV s^{-1}. Heterogeneous electron transfer (HET) rates were investigated by performing five cyclic voltammograms (CVs) in 10 mM K4Fe(CN)6/K3Fe(CN)6 (BioUltra ≥99.5%, Sigma–Aldrich) electrolyte supported by a pH 7.2 phosphate buffer (50 mM potassium phosphate monobasic/potassium phosphate dibasic trihydrate, ≥99%, Sigma–Aldrich) at scan rates ranging from 10 to 300 mV s^{-1}. All electrolytes were freshly prepared with ultrapure water (resistivity not less than 18.2 MΩ cm, Millipore Milli-Q Direct 8). An oxygen-free environment was achieved by vigorous N_2 bubbling (Oxygen-free grade, BOC Gases plc) prior to each electrochemical experiment, and maintained under positive N_2 pressure. All electrochemical glassware was cleaned overnight by soaking in a solution of dilute $KMnO_4$ (ACS ≥99%, Sigma–Aldrich) in concentrated H_2SO_4 (>95% analytical grade, Fisher Scientific), followed by thorough rinsing with ultrapure water.

Elucidation of heterogeneous electron transfer rate constants (k^O_{app}) was conducted by correlating the peak to peak separation of the K4Fe(CN)6/K3Fe(CN)6 redox features with the dimensionless parameter ψ. This was performed using two methods reported in the literature: Nicholson and Shain [45], and Klinger and Kochi [46] (see ESI). A diffusion coefficient of 7.26×10^{-6} cm^2 s^{-1} for the $[Fe(CN)6]^{3-/4-}$ redox pair was used in the calculation [47], assuming a charge transfer coefficient (α) of 0.5. The least squares linear regression of the HER peak current density (j_P) vs. the square root of the scan rate ($\upsilon^{1/2}$) was fitted with the Randles–Ševčík expression for irreversible redox processes [48] using $\alpha = 0.27$ (WS_2) and $\alpha = 0.3$ (MoS_2), both obtained after modelling the HER CVs obtained at 10, 50 and 100 mV s^{-1} scan rates with the DigiElch 7 software (Gamry Instruments Ltd., USA) according to a planar geometry.

3. Results and discussion

3.1. Fabrication and characterization of nanocone arrays

Compact monolayers of 220 nm diameter polystyrene nanospheres were deposited as described in Section 2.1 on both MoS_2 and WS_2 crystals and SEM micrographs taken to confirm high coverage and compactness (see Figure S1, ESI). The effects of plasma etching parameters on the NS-modified TMD crystals were then investigated. The initial isotropic oxygen plasma etching step was equivalent for all samples (40 s, 100 W RF power), whilst the duration of the subsequent anisotropic SF_6/C_4F_8 plasma etching step was varied to explore the influence of the plasma exposure time on the final surface nanopattern. Table 1 lists the etching parameters used and nanopillar dimensions obtained for MoS_2 and WS_2 crystals measured from SEM micrographs (typical images are shown in Fig. 1).

Significant variations in morphology were found on varying the etching time. For MoS_2, short etching times (Fig. 1a) created closely-spaced arrays of cylindrical pillars, whereas longer times resulted in arrays of cones with negligible interspacing. In

Table 1
Compilation of height (h_{nanoc}), diameter and interspacing of the nanopillars obtained after plasma etching of MoS_2 and WS_2 crystals as a function of the SF_6/C_4F_8 plasma etching time. Etching time inaccuracy is related to the one second high ICP power and flow rate "strike step" required for the formation of the SF_6/C_4F_8 plasma.

Material	SF_6/C_4F_8 plasma etching time/s	Angle-corrected nanopillar height/nm	Nanopillar diameter/nm	Nanopillar interspacing/nm	Aspect ratio	Radial coordinate, *R*	Normal coordinate, *Z*	Figure
MoS_2	15 ± 1	270 ± 20	200 ± 30	23 ± 1	1.3 ± 0.3	1.3	2.7	Fig. 1a
	32 ± 1	380 ± 40	200 ± 10	17 ± 5	1.9 ± 0.3	1.2	3.8	Fig. 1b
	38 ± 1	360 ± 20	190 ± 10	42 ± 3	1.9 ± 0.2	1.4	3.8	–
	45 ± 1	250 ± 20	110 ± 10	23 ± 1	2.4 ± 0.2	1.4	4.5	Fig. 1c
	60 ± 1	580 ± 20	230 ± 40	9 ± 1	2.5 ± 0.5	1.2	5.0	Fig. 1d
WS_2	16 ± 1	300 ± 20	110 ± 10	110 ± 10	2.8 ± 0.3	2.3	5.5	Fig. 1e
	31 ± 1	350 ± 30	110 ± 10	81 ± 4	3.1 ± 0.3	2	6.4	Fig. 1f
	31 ± 1	380 ± 30	150 ± 20	34 ± 4	2.5 ± 0.3	1.4	5.1	–
	46 ± 1	180 ± 20	140 ± 20	57 ± 7	1.3 ± 0.3	1.6	2.6	Fig. 1g
	61 ± 1	–	–	–	–			Fig. 1h

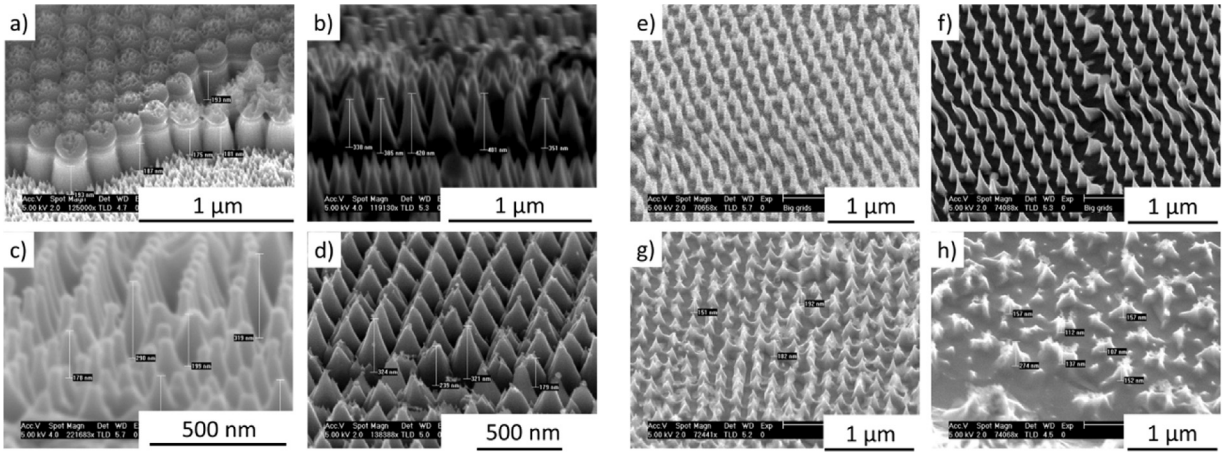

Fig. 1. FE-SEM micrographs of SF_6/C_4F_8 plasma-etched MoS_2 crystals for a) 15 ± 1 s (45° tilt angle), b) 32 ± 1 s (80° tilt angle), c) 45 ± 1 s (85° tilt angle) and d) 60 ± 1 s (45° tilt angle) and SF_6/C_4F_8 plasma-etched WS_2 crystals for e) 16 ± 1 s, f) 31 ± 1 s, g) 46 ± 1 s and h) 61 ± 1 s (all imaged at 45° tilt angle). Image distortion in e) and f) is attributed to SEM distortions: such areas are not considered during nanopattern characterization.

addition, a nanopillar height maximum was achieved at approx. 30 s (Fig. 1b), indicating that the SF_6/C_4F_8 etching could be subdivided into two regimes.

The first regime (<30 s etching time) involved both the MoS_2 etching as well as the etching of the remaining shrunken NSs monolayer. The transition from a nanocylinder array to a nanocone array, observed between 15 and 30 s etching, was driven by the survival of partially etched NSs. In this regime, the slower NS erosion rate compared with MoS_2 appears to cause SF_6/C_4F_8 plasma etching of MoS_2 material to occur by a 'side-on' mechanism, leading to conical structures with increased aspect ratios; higher etching times lead to higher nanopillar heights.

The second regime (>30 s etching time) occurs when the NSs have been fully etched away, leaving the conical array structures uncovered. This resulted in a preferential etching of the more reactive top section of the nanocones leading to a truncated nanocone array (see Fig. 1c). As a consequence, in this regime higher etching times led to lower nanopillar heights with increased aspect ratios. Depletion of highly-reactive nanocone tips at very long etching times (Fig. 1d) ultimately resulted in a top-down governed etching, obtaining very large nanopillars (>500 nm tall) with high aspect ratios.

For WS_2 crystals, all etching times led to nanocone array morphologies with a clear interspacing. Theoretical hardness values (based on Vickers' indentation method) would seem to indicate that bulk WS_2 is a harder material than bulk MoS_2 (HV_{max} values of 10 391 and 9703 MPa respectively) [49]. However, the shorter and further interspaced nanocones present in plasma-etched WS_2 compared to those found in MoS_2 at equivalent low etching times (Fig. 1e and f), suggest a higher chemical reactivity (i.e. dissolution rate) of WS_2 to the SF_6/C_4F_8 plasma. This higher horizontal etching rate compared to MoS_2 then justifies the narrower nanocone diameters found at short etching times: 110 ± 10 nm (WS_2) vs. 200 ± 30 nm (MoS_2) for 15 ± 1 s SF_6/C_4F_8 plasma etching. An increase in etching time generated taller nanocones with shorter interspacings: this reflects a shift from a 'side-on' to a top-down etching profile. At long etching times (>45 s), the faster WS_2 etching rate results in the deformation of the array structure (Fig. 1g) to form ultimately an amorphous structure (Fig. 1h), preventing the formation of truncated nanocone array structures.

XPS measurements were acquired to evaluate changes in the WS_2 samples' surface composition after plasma etching (Fig. 2, see Table S1 and Fig. S2 ESI for detailed analysis), in order to compare our previous results obtained on equivalent plasma-etched MoS_2 [40]. The high-resolution W *4f* spectra of the as-received WS_2 crystal presents the characteristic W $4f_{7/2}$:$4f_{5/2}$ spin–orbit doublet of the semiconducting 2H phase (Fig. 2a, binding energies of ~32.65 and ~34.8 eV, respectively) [50], with no observable contribution from any other WS_2 phases (1T) or W compounds (WO_x), whereas the S *2p* spectra exhibits the S $2p_{3/2}$:$2p_{1/2}$ spin orbit doublet (Fig. 2b, 162.3 and 165.1 eV, respectively) from the S^{2-} oxidation state [51], giving a W:S ratio of 1:2.0 ± 0.1 expected for crystalline WS_2 [52].

The XPS spectra for the freshly plasma-etched samples present, on the other hand, additional surface components. In the case of the W *4f* region (Fig. 2c), spin–orbit doublets arising from the 1T phase (~31.65 and ~33.8 eV) and from WO_2 (~33.0 and ~35.2 eV) [53] can be detected. For the S *2p* region (Fig. 2d), an additional broad signal centred at ~168 eV is found, related to S high oxidation states

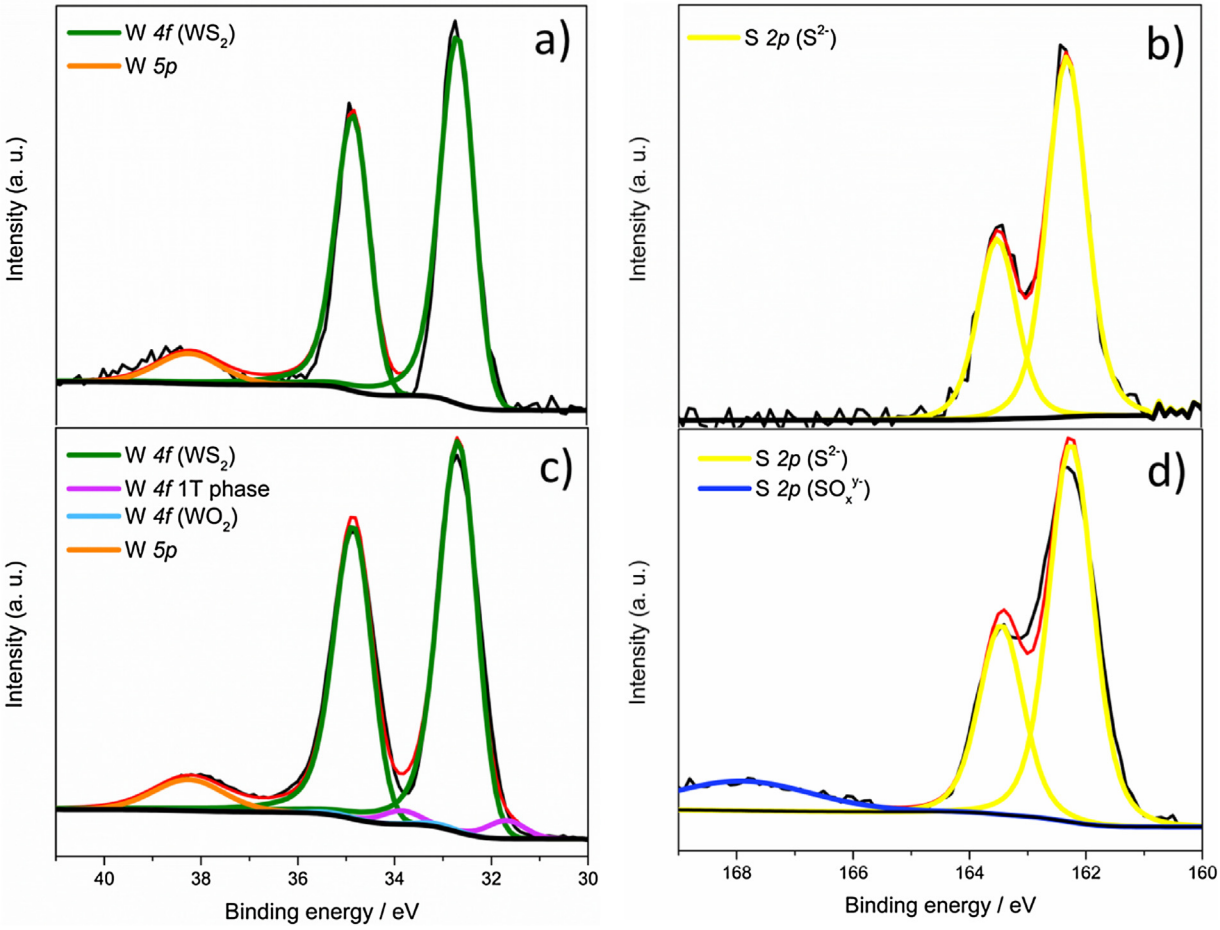

Fig. 2. High-resolution XPS spectra of W 4f (left) and S 2p (right) regions for as-received (top) and 31 ± 1 s, R = 1.4, Z = 5.1 (bottom) SF_6/C_4F_8 plasma-etched WS_2 crystals. Labels: W^{4+} $4f_{7/2:5/2}$ WS_2 2H phase (green), W^{4+} $4f_{7/2:5/2}$ WS_2 1T phase (magenta), W^{4+} $4f_{7/2:5/2}$ WO_2 (light blue), W 5p (orange), S $2p_{3/2:1/2}$ from S^{2-} (yellow) and S 2p from SO_x^{y-} (dark blue). (For interpretation of the references to colour in this figure legend, the reader is referred to the web version of this article.)

widely ascribed to SO_x^{y-} species [54,55]. Thus, plasma-etching promotes the exposure of metallic 1T sites, presumably located at the nanopillars' surface, but also a conversion of a small fraction of WS_2 to WO_2. The latter is supported by an increase in the relative content of oxidized SO_x^{y-} species vs. S^{2-} species as the plasma-etching time increases (from 0% at t = 0–19.9% at t = 61 ± 1 s, see Table S1 ESI). Compared to WS_2, however, previously reported freshly-fabricated plasma etched MoS_2 nanocone arrays present significantly higher MoO_x surface contents, with $MoS_2/MoO_2/MoO_3$ relative XPS molar percentages of 56.1/35.8/8.1 [40]. This can be understood by the well reported MoS_2 high reactivity with RF-oxygen [56] and ICP SF_6-based plasmas [57]: these treatments generate structural damage within the MoS_2 crystallite (e.g. broadening of the A_{1g} and $E^1{}_{2g}$ Raman vibration modes) [58] and formation of oxygen-containing MoO_xS_y species [59]. Such oxygen incorporation can be understood by the low energies required to form sulphur vacancies (2.12 eV) [60] which can be surpassed, for electrons generated by SF_6-based plasmas, with power densities as low as ~1.5 mW cm^{-3} [57]. Thus, despite of exhibiting a slight broadening of the W $4f_{7/2}$:$4f_{5/2}$ FWHM values (~0.8 eV pristine vs. ~0.9 eV plasma-etched), WS_2 seems to present a minor structural damage and consequently a lower oxygen incorporation after plasma-etching.

The relatively low 1T phase contents for plasma-etched WS_2 samples (≤4%, Table S1 ESI) can be explained by the intrinsic surface-sensitive nature of XPS. As the average XPS maximum photoelectron space depth is of ca. 10 nm, XPS can only probe the outermost surface of the hundreds of nanometers-thick WS_2 nanocone arrays (i.e. the nanocones' tip surface). Thus, XPS cannot quantify the 1T sites present at the nanocones' lower regions, which should be main contributors for both surface area and HER catalysis. Further evidence can be drawn from the actual 1T phase percentages obtained: highest 1T contents were found in the sample with lower aspect ratio (ca. 4.4% for 31 ± 1 s, aspect ratio = 3.1 ± 0.3) and vice versa (ca. 0.9% for 31 ± 1 s, aspect ratio = 2.5 ± 0.3), which contradicts the expected behaviour of higher 1T site contents at higher aspect ratio structures. This can be understood by the wider nanocone tip surfaces found in structures with lower aspect ratios; these imply larger exposed areas at the sub-10 nm region than the sharp structures found in high aspect ratio nanocones, justifying the higher XPS 1T contents found in lower aspect ratio structures.

3.2. *Electrocatalytic activity for the hydrogen evolution reaction (HER)*

Plasma-etched MoS_2 and WS_2 crystals were electrochemically tested in a 2 mM $HClO_4$/0.1 M $NaClO_4$ aqueous electrolyte to investigate the electrocatalytic enhancement of the hydrogen evolution reaction (see Section 1.3 ESI for further information about electrolyte). Two main voltammetric features can be observed in the cathodic region with this electrolyte: a diffusional reduction wave at ca. -0.3 to -0.7 V (vs. NHE) due to the 2 mM proton concentration followed by bulk solvent breakdown at ca. 300–400 mV higher overpotentials. The characteristic proton diffusion decay profile observed in this electrolyte, despite of not enabling to achieve the typical 10 mA cm^{-2} benchmarking current densities reported for TMDs, will enable to discern mass transport properties arising

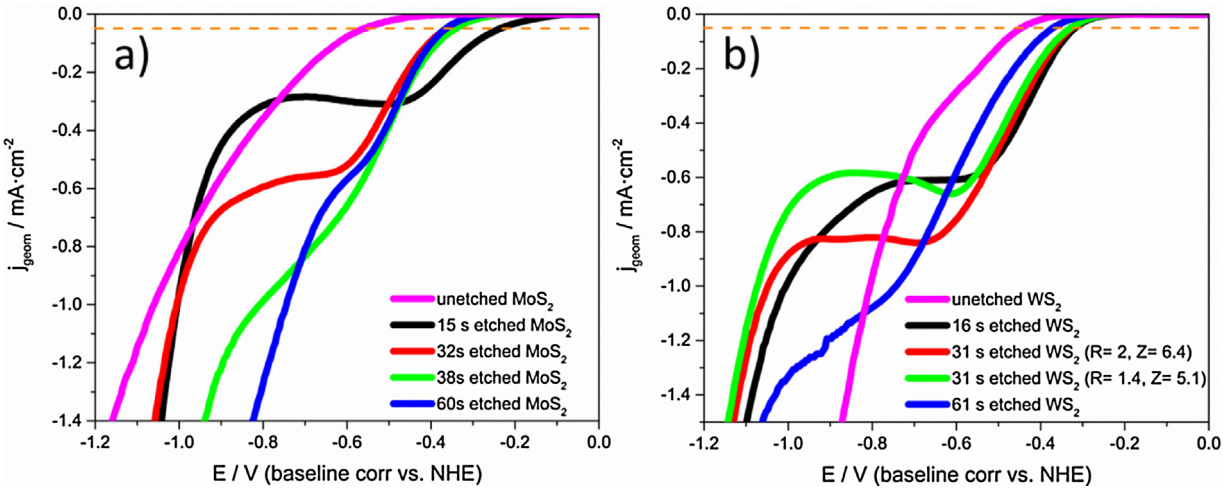

Fig. 3. Linear sweep voltammograms of SF_6/C_4F_8 plasma-etched a) MoS_2 and b) WS_2 crystals in the 0 to −1.2 V voltage range vs. NHE. Dashed line (orange) indicates j_{geom} = 0.05 mA cm^{-2} (see text). Voltage scan rate: 50 mV s^{-1}. (For interpretation of the references to colour in this figure legend, the reader is referred to the web version of this article.)

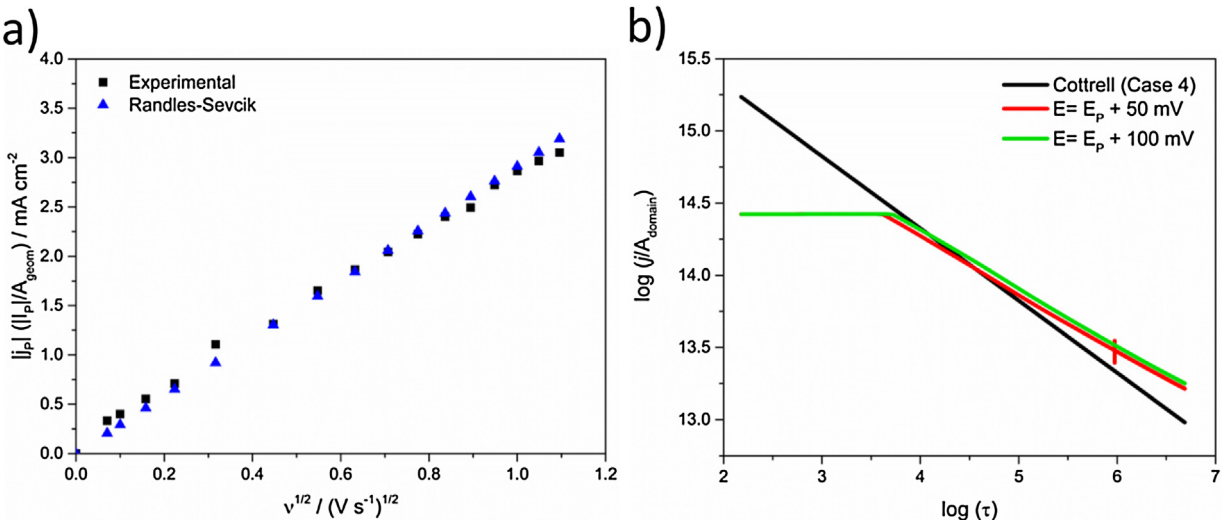

Fig. 4. 15 ± 1 s plasma-etched MoS_2 crystal a) geometric peak current density j_P vs. square root of the scan rate $\upsilon^{1/2}$ plots for HER experimental (black) and theoretical values predicted by the irreversible Randles–Ševčík equation (blue); b) HER experimental (red = E_P + 50 mV; green = E_P + 100 mV) and theoretical irreversible Randles–Ševčík case 4 (black) log–log plots of transient dimensionless current densities j/A_{domain} vs. dimensionless time τ. (For interpretation of the references to colour in this figure legend, the reader is referred to the web version of this article.)

from the nanoarray geometries under study. These effects are vital in understanding the interplay between pure catalytic effects and mass transport, which would be masked at higher proton concentrations (i.e. 0.5 M H_2SO_4).

Fig. 3 shows the linear sweep voltammograms (LSVs) obtained for as-received (unetched) as well as plasma-etched MoS_2 and WS_2 for different etching times at 50 mV s^{-1} scan rate. In both materials a shift in the HER onset potential is observed compared with the unetched samples, ≈200 mV for MoS_2 (−0.56 to −0.36 V) and ≈100 mV for WS_2 (−0.44 to −0.34 V), where the onset is measured at a HER current density of 0.05 mA cm^{-2} (see dashed line in Fig. 3). The maximum HER shift is observed for the 15 s etched MoS_2 sample, ≈320 mV from −0.56 to −0.24 V. This indicates that the plasma etching treatment successfully exposes an increased number of active sites by generation of an edge-abundant nanopillar array, being more effective for MoS_2 than for WS_2.

For equivalent etching times, the WS_2 samples exhibit higher steady-state current density values than MoS_2 at a given scan rate (Fig. 3, Fig. S3 ESI). In order to discern if the origin of the enhanced HER currents in WS_2 samples is due to kinetic or mass transport effects derived from the high-aspect ratio nanoarrayed structures, we analyzed the HER peak current variation with voltage scan rate (Randles–Ševčík equation) for the tested samples. Previous investigations on cylindrical micropillar [61,62] and microdisc [63,64] electrode arrays concluded that four different diffusional mass transport regimes could be distinguished, depending upon microelectrode height, radius and interelectrode distances [64]. All samples tested here, based on both nanopillar dimensions and experimental timescales, should satisfy case 4 where the diffusion layer thickness (δ) is larger than both the size and interspacing of the microelectrodes, resulting in a complete overlap of the microelectrode diffusion layers towards a semi-infinite planar diffusion regime, characteristic of macroelectrodes.

The experimental peak current (plotted here as geometric current densities $j_P = I_P/A_{geom}$ for normalization purposes) vs. square root of the scan rate ($\upsilon^{1/2}$) plots of plasma-etched MoS_2 crystals (Fig. 4a, Fig. S4 ESI) are in excellent agreement with those predicted by the irreversible Randles–Ševčík expression for a planar electrode of equivalent geometrical area, irrespective of the scan rate studied. This would indicate that neither the contribution

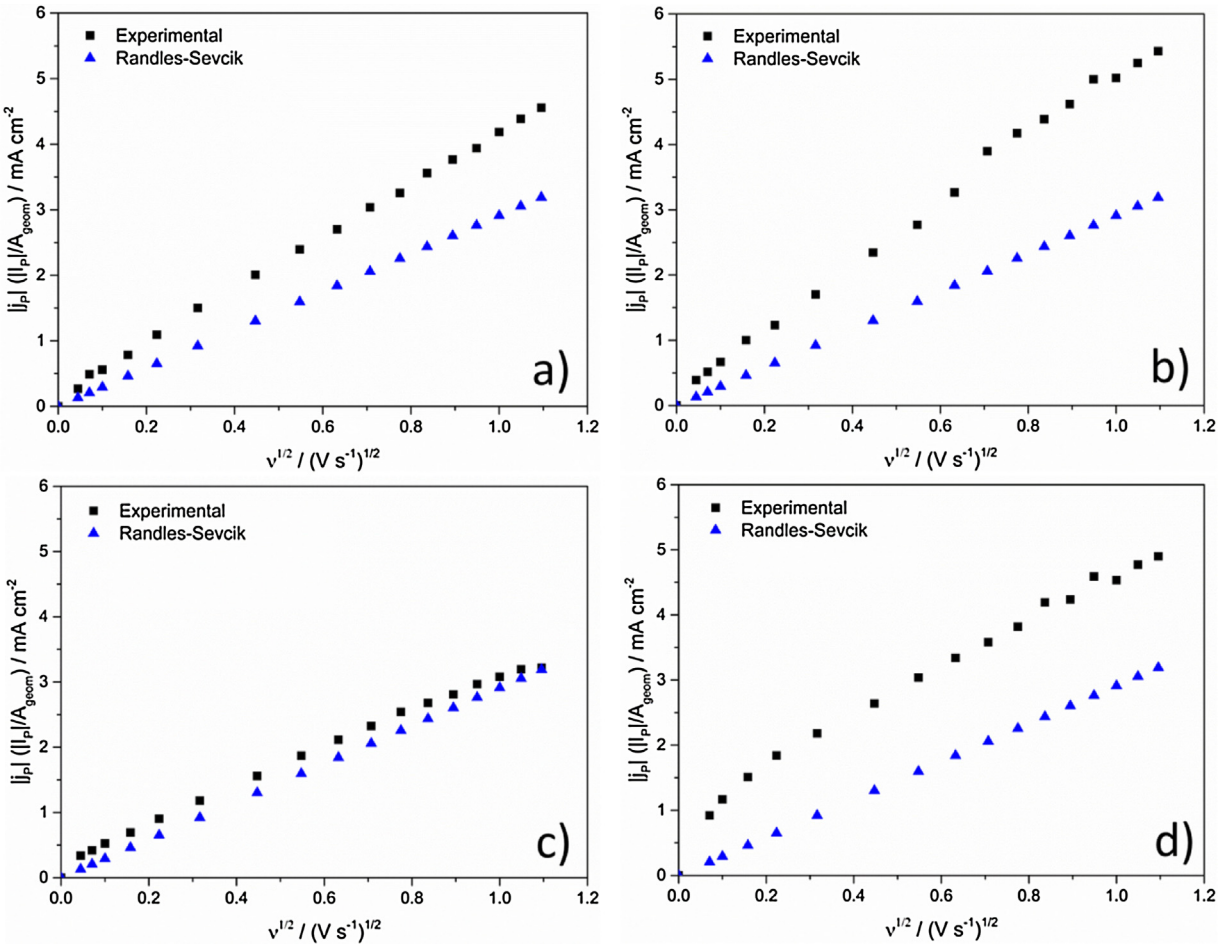

Fig. 5. Plasma-etched WS_2 crystals geometric peak current density j_P vs. square root of the scan rate $\upsilon^{1/2}$ plots for HER experimental (black) and theoretical values predicted by the irreversible Randles–Ševčík equation (blue). Etching conditions: a) 16 ± 1 s, b) 31 ± 1 s (R = 2, Z = 6.4), c) 31 ± 1 s (R = 1.4, Z = 5.1) and d) 61 ± 1 s. (For interpretation of the references to colour in this figure legend, the reader is referred to the web version of this article.)

of the nanopillars to the overall HER current with respect to the MoS_2 crystal geometrical area, nor possible pseudo-thin layer mass transport effects are significant. The radial diffusion profiles formed at individual nanocone overlap due to the narrow nanocone interspacing (≤40 nm), resulting in an overall semi-infinite planar diffusion regime (case 4 behaviour, see above). Therefore, any HER enhancement observed for these samples is due to the exposure of active edge sites rather than to a mass transport enhancement.

The experimental geometric peak current density (j_P) vs. $\upsilon^{1/2}$ plots for plasma-etched WS_2 crystals show increased current densities with respect to the theoretical irreversible Randles–Ševčík HER peak current densities of an equivalent planar electrode (Fig. 5). These effects are more noticeable for samples with higher aspect ratios and at faster scan rates (υ > 50 mV s^{-1}), in apparent contradiction of the expected case 4 behaviour deriving from the microelectrode array model [65].

In the downsizing from the microelectrode to the nanoelectrode scale, however, the equivalency and diffusional independence of each nanoelectrode in the array might no longer be satisfied. Investigations by Godino et al. on the concentration profiles of recessed nanoelectrode arrays with radius r = 50 nm and diameter d = 1000 nm at a scan rate υ = 1 V s^{-1} revealed that complete overlapping of the individual nanoelectrode diffusion layers led to a hemispherical diffusion layer characteristic of a microelectrode, contrary to the case 4 scenario predicted for an equivalent microelectrode array [66]. This indicated that, despite being diffusionally independent, the nanoelectrodes in the array are no longer equivalent, and that radial diffusion can be more important in nanoelectrode arrays than in microelectrode arrays.

A computational model accounting for the diffusional field overlapping of adjacent nanoelectrodes in an array was recently proposed, with improved prediction capability [67]. Further experimental investigations of scan rate, nanoelectrode interspacing and population effects confirmed the discrepancies with the microelectrode array behaviour. These are summarized as follows: i) slow scan rates (υ < 1 V s^{-1}) enhanced the degree of nanoelectrode diffusion field overlap and inequality, favouring an overall microelectrode response, ii) larger interspacings promoted the diffusionally independent behaviour of each nanoelectrode in the array at a given scan rate, and iii) very densely populated arrays promoted, at slow scan rates, an unequal performance between nanoelectrodes in the inner positions and those in the nanoarray perimeter, where the inner nanoelectrodes resembled the behaviour predicted by the diffusion domain approximation [66].

Accordingly, this indicates that the overall macroelectrode response obtained for the plasma-etched MoS_2 crystals is mainly due to the densely-packed nanopilllar array geometries obtained, irrespective of the etching time and aspect ratio. The highly overlapped diffusional layers generated by each nanopillar induced by the short interspacings (≤40 nm) along with the large dimensions of the MoS_2 crystal (i.e. high density of inner nanopillars) would counterbalance the radial diffusion contribution of the perimetric nanopillars in the overall HER current. Thus, it is hypothesized that only at very fast scan rates will the nanopillars exhibit diffusionally

Table 2
Definition of dimensionless parameters used for transient chronoamperometry experiments.

Parameter	Expression
Diffusion domain area, A_{domain}	d^2
Diffusion domain radius, r_{domain}	$\sqrt{d^2/\pi}$
Radial coordinate, R	r_{domain}/r_{nanoc}
Normal coordinate, Z	h_{nanoc}/h_{nanoc}
Dimensionless time, τ	$D_H + t/r_{nanoc}^2$
Dimensionless current, j	$I/(2\pi F C_{H^+,bulk} D_{H^+} r_{nanoc})$

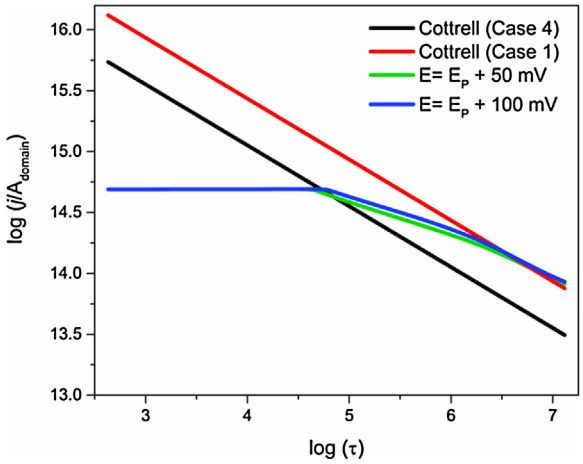

Fig. 6. 31 ± 1 s (R = 2, Z = 6.4) plasma-etched WS_2 crystal HER experimental (red = E_P + 50 mV; green = E_P + 100 mV) and theoretical (black, irreversible Randles–Ševčík case 4; red, irreversible Randles–Ševčík case 1) log–log plots of transient dimensionless current densities j/A_{domain} vs. dimensionless time τ. (For interpretation of the references to colour in this figure legend, the reader is referred to the web version of this article.)

independent layers resembling the behaviour of cases 1 and 2 for microelectrode arrays [66].

For the plasma-etched WS_2 samples, the clear correlation between increased HER peak current densities and higher aspect ratios at the investigated scan rates rules out an explanation solely based on the nanoarray population density. The WS_2 samples etched for 16 s (R = 2.3, Z = 5.5) and 31 s (R = 2.0, Z = 6.4) exhibit higher HER peak currents, the latter being the highest despite a smaller nanocone interspacing. This indicates that, apart from the smaller degree of overlap of the nanocone diffusion layers with respect to the MoS_2 samples, WS_2 nanocones with higher aspect ratios could present a larger contribution of radial diffusion as well as a higher abundance of active edge sites, leading to higher HER currents. These findings would be consistent with effects i) and ii) mentioned previously, as well as with the smaller diffusional overlap predicted for higher aspect ratio nanocone arrays at a given scan rate [68].

However, for the other 31 s-etched WS_2 sample (R = 1.4, Z = 5.1), the densely packed nanocone arrays obtained (interspacing ≈35 nm) lead to j_P values similar to those predicted by the irreversible Randles–Ševčík expression, leading to an overall quasi-planar electrode performance similar to the MoS_2 etched samples. This suggests that the nanopillar interspacing is the governing factor for obtaining nanocone array diffusion regimes different from case 4, as the MoS_2 etched samples exhibit similar nanopillar heights but smaller aspect ratios than the plasma-etched WS_2 counterparts. The effect of the maximized radial diffusion flux to the nanocone apex for low α' values ($\alpha' \leq 10°$, where α' is defined as the angle between the nanocone surface and its vertical axis) and its contribution to the overall HER current should be minimal compared with that of the nanocones' surface, as current is radius-dependent, and at the apex $r \approx 0$, supporting the key role of the nanocone interspacing in the overall diffusion regimes [68].

Transient chronoamperometry experiments at potentials beyond that of the HER peak current (+50–100 mV) were performed to gain further insight on the mass transport regimes present at short timescales (t < 5 s). Dimensionless log–log plots of experimental current density vs. time are shown in Figs. 4b, 6 and S4b and S5, along with the theoretical current plots for microelectrode arrays cases 1 and 4 (see Section 2.4 ESI): definitions of the dimensionless parameters used in the diffusion domain approximation are compiled in Table 2. The zero gradient regions observed at short timescales (t < 10 ms for MoS_2 and t < 300 ms for WS_2) are ascribed to non-Faradaic capacitive currents [48].

The response of the MoS_2 etched samples (Fig. 4b and S4b) seems to converge with the currents predicted by case 4, departing from a Cottrellian regime (characterized by a log–log slope of −1/2) at short timescales through a transitional mass transport regime. The slope and extent of the transitional regime are reported to be intimately linked to nanopillar density and dimensions (radius and height), and thus are difficult to explain experimentally based on dimensionless parameters [62]. Experimental discrepancies with respect to case 4 could be ascribed to the modification of the geometric area and nanocone geometry by electrochemically-induced restructuring under HER experiments.

Analogous experiments on the WS_2 samples revealed, beyond the capacitive charging current, an absence of Cottrellian behaviour at short timescales followed by a transitional mass transport regime as observed in the MoS_2 samples. For the 31 s (R = 2.0, Z = 6.4) etched WS_2 sample (Fig. 6), the experimental current converges to the calculated current with a slope of ca. −1/2, indicating that macroscopically the sample behaves with an overall planar diffusion to the nanocones and intercone surfaces and therefore has an electroactive area equivalent to the real surface area.

The 16 s (R = 2.3, Z = 5.5) sample (Fig. S5a) exhibits experimental currents significantly higher than those predicted for planar diffusion, confirming the additional current contribution from radial diffusion. This suggests that the enhanced HER current of the 31 s etched sample vs. the 16 s etched sample is due to their nanocone larger aspect ratio which exposes more HER active sites rather than to a synergistic contribution from enhanced mass transport.

Finally, for the other 31 s etched WS_2 sample (R = 1.4, Z = 5.1), the experimental current divergence from cases 1 and 4, having a log–log slope of approx. −1/4, which suggests a complex mass transport behaviour at short timescales (Fig. S5b). We hypothesize that at longer timescales this would ultimately converge to a quasi-case 4 behaviour, based on the experimental irreversible Randles–Ševčík plots forced by the narrow nanocone interspacing.

Tafel slope analysis was performed to elucidate the HER efficiency of the catalysts and the HER reaction mechanism. Naturally occurring MoS_2 and WS_2 layers present Tafel slopes (b) of ≈120 mV dec^{-1}, characteristic of the Volmer mechanism in which the atomic hydrogen adsorption is the HER limiting step [69]. Pure 1T-phase MoS_2 [70], 1T-phase WS_2 and edge-rich nanosheet samples [71,72] were reported to exhibit slopes of ≈40 mV dec^{-1}, ≈55 mV dec^{-1} and ≈55–60 mV dec^{-1}, respectively.

By contrast, noble metals such as Pt display Tafel slopes of ≈30 mV dec^{-1}, following the Volmer–Tafel mechanism under which the desorption of molecular hydrogen is the reaction limiting step [73]. Tafel slope analysis (Fig. 7) of the 50 mV s^{-1} LSVs reveal that SF_6/C_4F_8 plasma-etched WS_2 samples, with the exception of the 31 ± 1 s etched sample, show Tafel slope values lower than their MoS_2 counterparts. Thus, the HER mechanism and efficiency of the geometrically accessible active edge sites is closer to the best performing HER catalysts in WS_2 than in MoS_2.

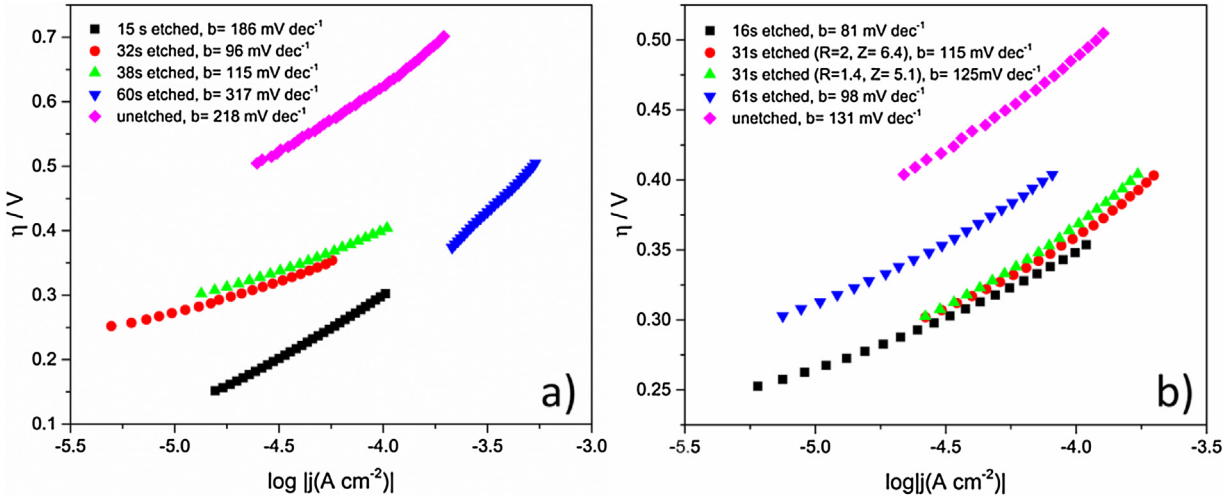

Fig. 7. Tafel plots (η vs. $\log|j_{geom}|$) of a) MoS_2 and b) WS_2 SF_6/C_4F_8 freshly plasma-etched crystals. Voltage scan rate: 50 mV s^{-1}.

For WS_2, values range between 80 and 125 mV dec^{-1}, indicating that the Volmer adsorption mechanism is the HER rate limiting step. Tafel plot values for MoS_2 are in some cases (unetched, 15 ± 1 s etched, 60 ± 1 s etched) higher than the $b \approx 120$ mV dec^{-1} value expected, indicating a high TMD through-plane resistance that hinders electron transfer kinetics. The high Tafel slope for unetched MoS_2 ($\approx$220 mV dec^{-1}) in comparison with unetched WS_2 ($\approx$130 mV dec^{-1}) confirms that the significant HER shift obtained after plasma etching is due to the initially low MoS_2 activity.

3.3. Electron transfer properties of plasma-etched TMDs

The experimental elucidation of electron transfer properties is essential to benchmark the inherent electrochemical properties of a material. Kinetic parameters have not been widely studied for TMDs [74–78] and are generally assessed by calculation of the (apparent) heterogeneous electron transfer (HET) constant k^O_{app} based on electrochemical experiments using redox mediators such as $Fe(CN)_6^{4-}/Fe(CN)_6^{3-}$ [47]. Thus, the k^O_{app} calculation should enable the intrinsic electron transfer properties of SF_6/C_4F_8 plasma-etched TMDs to be correlated with their experimental HER performance. Calculation of k^O_{app} was carried out using the Nicholson and Shain method (for $\Delta E_P < 220$ mV) [45] and the Klinger and Kochi analysis (for $\Delta E_P < 220$ mV) [46]; for further details see Section 2.5 ESI. Experimental ΔE_P values were obtained by performing cyclic voltammograms in an electrolyte containing the $Fe(CN)_6^{4-}/Fe(CN)_6^{3-}$ quasi-reversible redox mediator within scan rates of $\upsilon = 0.01$–0.3 V s^{-1}. This voltage window was selected to avoid overlapping with the inherent electro-oxidative TMD features at $E > +1.10$ V vs SCE and the HER onset at $E < -0.60$ V vs SCE. Experimentally recorded ΔE_P values at $\upsilon = 100$ mV s^{-1} and calculated k^O_{app} values obtained from the ψ vs. $[(\pi nFD\upsilon/RT)^{-1/2}]$ plot are summarized in Fig. 8 (see Table S2 for values, and Fig. S6 for Klinger and Kochi plot).

Two conclusions can be extracted from the results. First, the plasma-etched WS_2 samples present faster electron transfer kinetics ($k^O_{app} > 2.2 \times 10^{-5}$ cm s^{-1}) than the MoS_2 samples, irrespective of nanopillar dimensions and etching conditions. This supports the HER experimental evidence which suggested that plasma-etched WS_2 is an inherently more electrochemically active material. Secondly, there is a positive correlation between k^O_{app} values and the nanopillar height (see Fig. S7). This seems to indicate that a higher abundance of active edge sites in taller nanopillars improves the electron transfer properties of TMDs (reported k^O_{app} values of bulk MoS_2 and WS_2 are, respectively, 2.1×10^{-5} cm s^{-1} and $<6.3 \times 10^{-6}$ cm s^{-1}) [74,76,79], consistent with previous findings in the literature which correlated a higher exposure of the metallic 1T phase edge sites with enhanced electrical conductivities [51,70].

The enhanced performance of plasma-etched WS_2 vs. MoS_2 crystals lies on their relative stability towards the oxygen plasma employed in the nanosphere shrinking process. Previous XPS studies confirmed the incorporation of oxygen into 2H-MoS_2 single crystals upon RF-oxygen plasma exposure, converting the S^{2-} and Mo^{4+} initial states to S^{6+}, Mo^{5+} and Mo^{6+} characteristic of molybdenum sulfates ($Mo(SO_4)_2$), molybdenum oxysulfides (MoS_xO_y) and molybdenum oxides (Mo_xO_y), respectively [59]. Recent investigations in our group revealed that air exposed (>20 days) plasma-etched MoS_2 crystals presented an increased MoO_2 content to the detriment of MoS_2, achieving MoO_2/MoS_2 molar percentages of 51.97/45.52 [40]. In the case of WS_2, XPS studies on the electrochemically tested, atmosphere-exposed samples revealed a very low WO_2 content ($\leq$2%) [41], confirming their higher stability against oxygen incorporation from the RF-oxygen plasma step.

With regard to the effect of oxygen incorporation on the HER activity of MoS_2, Latiff et al. reported that incremental MoO_2 contents in physical mixtures with bulk MoS_2 worsened the HER performance [80], contrary to previous results obtained with oxygen-incorporated, few-layered MoS_2 [81]. Thus, despite observing an HER enhancement after plasma-etching arising from a higher abundance of edge sites, MoS_2 nanopillar arrays present slower electron transfer properties due to their oxygen impurities compared with the plasma-etched WS_2 samples, following the same behaviour observed for bulk MoS_2 [80].

3.4. Analysis of 5-month atmospherically aged samples

An investigation of the influence of air exposure and electrochemically-induced restructuring on the electrocatalytic activity was carried out by testing the SF_6/C_4F_8 plasma-etched WS_2 crystals after 5 months' preservation in a desiccator (Fig. 9a). WS_2 etched samples still present a shift in the HER onset potential compared with the unetched sample ($\approx$60 mV, from -0.47 to -0.41 V), but lower than the one observed for the fresh samples ($\approx$100 mV). This suggests a loss in the number of active edge sites due to electrochemical degradation, due for example to sample oxidation,

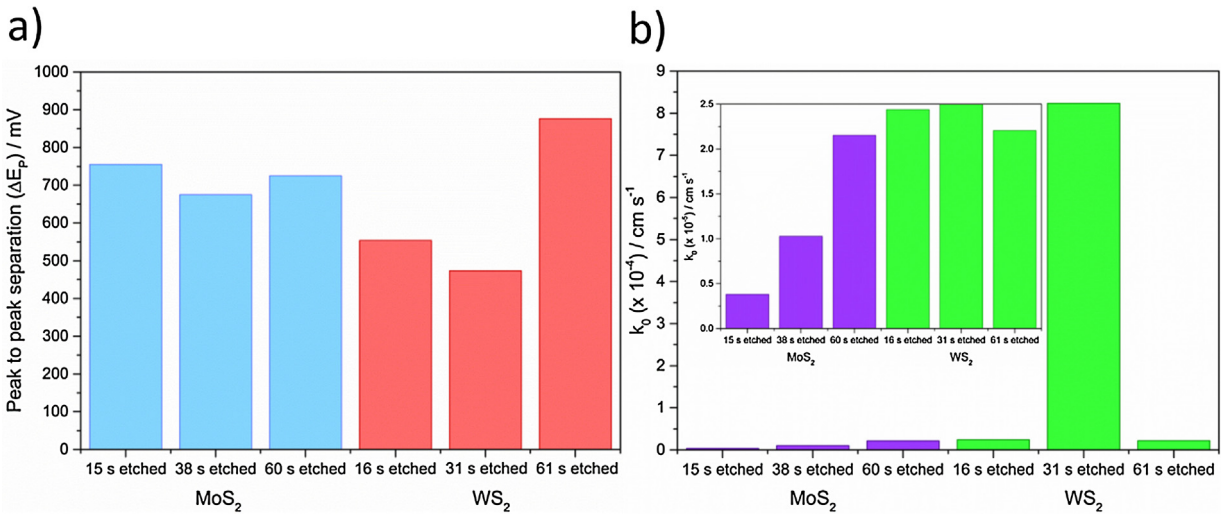

Fig. 8. a) Peak to peak separations of the ferro/ferricyanide redox probe for plasma-etched MoS_2 (blue) and WS_2 (red) samples at $\upsilon = 100\ mV\ s^{-1}$, b) heterogeneous electron transfer rate constants k^{O}_{app} calculation for plasma-etched MoS_2 (purple) and WS_2 (green) samples. Inset: zoom of 9b for a $k^{O}_{app} \times 10^{-5}$ cm s^{-1} scale bar to highlight MoS_2 values. (For interpretation of the references to colour in this figure legend, the reader is referred to the web version of this article.)

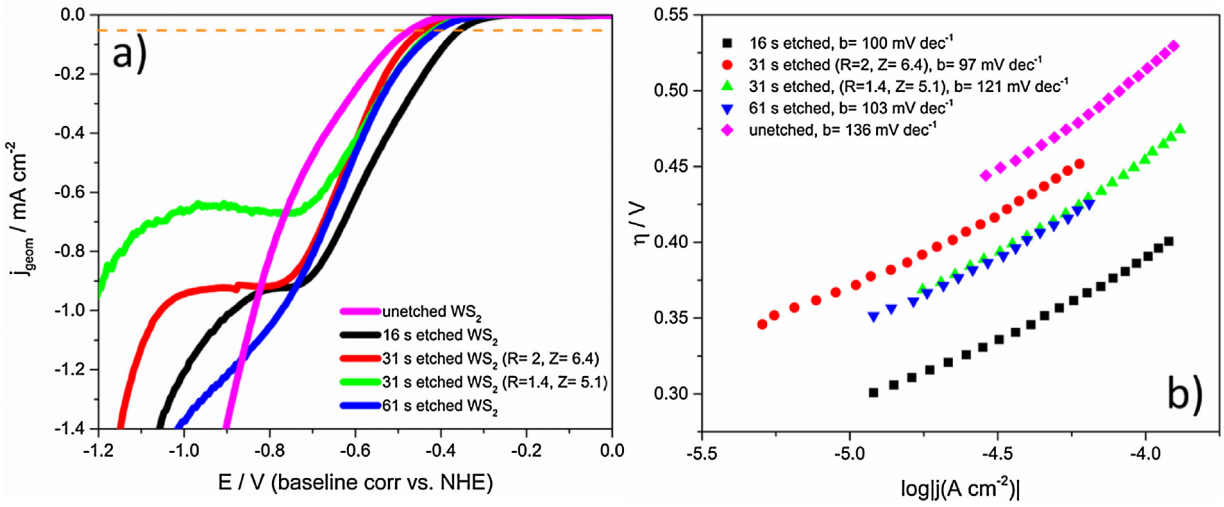

Fig. 9. a) Linear sweep voltammograms in the 0 to −1.2 V voltage range vs. NHE and b) Tafel plots (η vs. $\log|j_{geom}|$) for WS_2 atmospherically-aged SF_6/C_4F_8 plasma-etched crystals. Dashed line (orange) indicates $j_{geom} = 0.05\ mA\ cm^{-2}$ (see text). Voltage scan rate: $50\ mV\ s^{-1}$. (For interpretation of the references to colour in this figure legend, the reader is referred to the web version of this article.)

as reported previously [75,82]. Comparison of LSVs obtained from fresh and aged etched WS_2 samples reveals a significant increase in current density values for samples subject to short etching times (Fig. 10a and b), whereas samples etched for long times present a similar current density plateau but shifted to higher overpotentials (Fig. 10c and d). Tafel plot analysis (Fig. 9b) supports these results, as short etching time samples exhibit a lower Tafel slope after ageing (≈20 mV dec^{-1} lower for 31 ± 1 s ($R = 2$, $Z = 6.4$) etched sample), in contrast to the almost invariant Tafel slopes obtained for long etching time, aged samples (variations less than ≈5 mV dec^{-1}). The 16 ± 1 s etched WS_2 sample presents a higher current density plateau despite exhibiting a higher Tafel slope (100 mV dec^{-1} vs. 81 mV dec^{-1}).

We postulate that the electrochemical cycling cannot fully penetrate or restructure the tall, short interspaced nanocone arrays and amorphous morphologies obtained at long etching times but removes some active edge sites. This results in a minimal modification of morphology and active edge sites HER kinetics leading to a similar LSV profile shifted to higher overpotentials. On the other hand, both short and widely interspaced nanocone arrays are more prone to electrochemically-induced restructuring, leading to higher surface areas with lower active edge site densities. SEM micrograph analysis (Fig. S8 ESI) of the samples after electrochemical testing (Table 3) supports this: briefly etched samples exhibited significant modifications in the nanocone aspect ratio (for 16 ± 1 s, an increase from 2.8 ± 0.3 to 3.9 ± 0.4; for 31 ± 1 s with $R = 2.0$, $Z = 6.4$, a decrease from 3.1 ± 0.3 to 1.9 ± 0.2), while long-etched samples show almost invariant nanocone dimensions and morphologies. The evident modification in HER activity observed after short duty electrochemical tests suggests, then, that the plasma-etched TMD nanocone array nanostructures are indeed prone to surface modification under HER operating conditions due to electrochemical restructuring, this foreseeable to worsen at long operating times. Long term electrochemical testing of these samples are, consequently, out of the scope of this paper, as our focus is drawn to the nanocone array morphology role in the inherent mass transport and HER voltammetric profile, which is irreversibly altered if successive cycling experiments are performed [41].

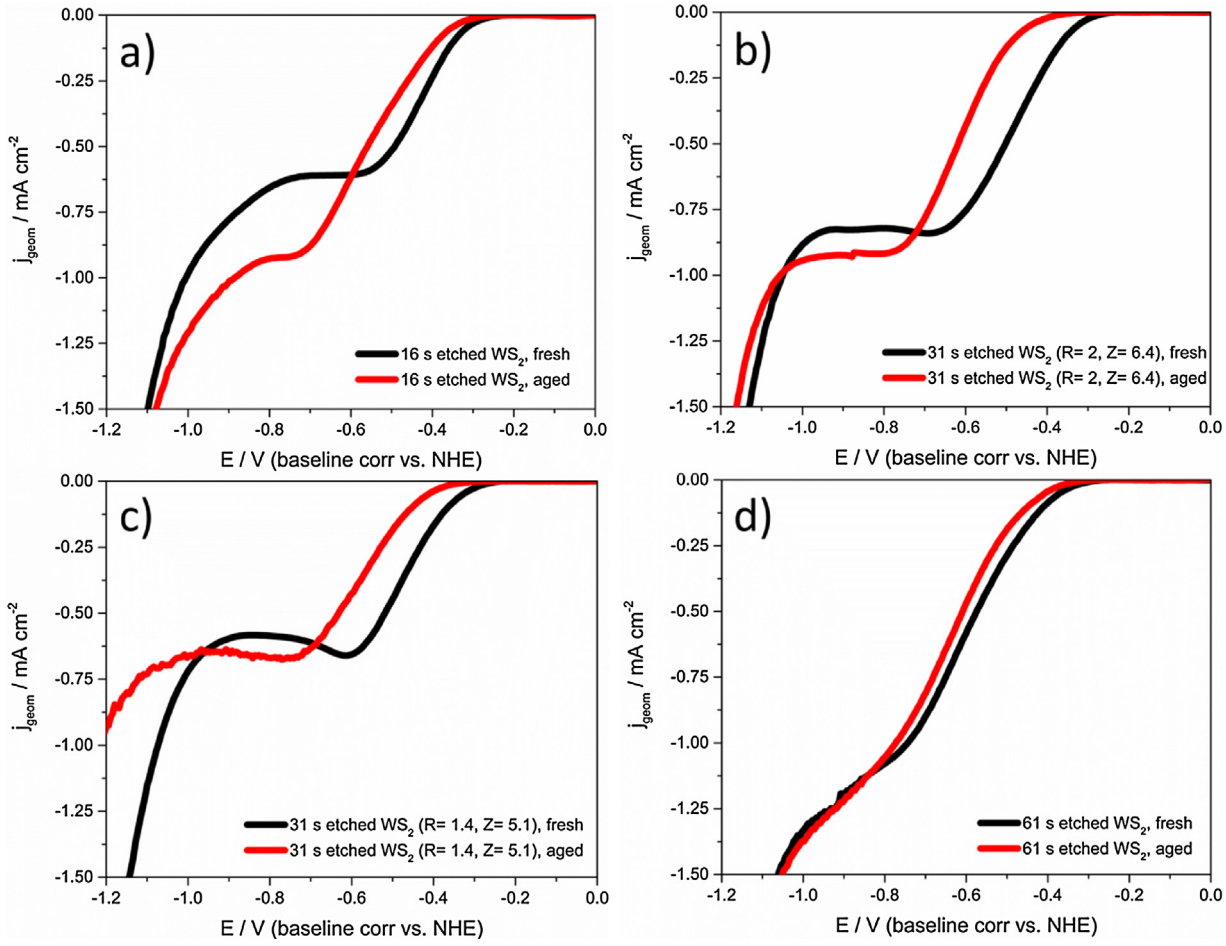

Fig. 10. Comparison of HER performance of a) 16 ± 1 s, b) 31 ± 1 s (R = 2, Z = 6.4), c) 31 ± 1 s (R = 1.4, Z = 5.1) and d) 61 ± 1 s SF_6/C_4F_8 plasma-etched fresh (solid black) and 5-month aged (solid red) WS_2 crystals in the 0 to −1.2 V voltage range vs. NHE in 2 mM $HClO_4$/0.1 M $NaClO_4$. Voltage scan rate: 50 mV s^{-1}. (For interpretation of the references to colour in this figure legend, the reader is referred to the web version of this article.)

Table 3
Compilation of height, diameter and interspacing of the nanopillars obtained after plasma etching and 5-month atmosphere exposure of WS_2 crystals as a function of the SF_6/C_4F_8 plasma etching time.

Material	SF_6/C_4F_8 plasma etching time/s	Angle-corrected nanopillar height/nm	Nanopillar diameter/nm	Nanopillar interspacing/nm	Aspect ratio	R	Z
Aged WS_2	16 ± 1	420 ± 30	100 ± 10	75 ± 8	3.9 ± 0.4	2	8.4
	31 ± 1	240 ± 30	125 ± 10	87 ± 9	1.9 ± 0.2	1.9	3.8
	31 ± 1	320 ± 20	120 ± 10	62 ± 8	2.7 ± 0.3	1.7	5.3
	61 ± 1	–	–	–	–	–	–

4. Conclusions

Edge-abundant MoS2 and WS2 nanopillar arrays have been successfully fabricated by nanosphere lithography and plasma etching treatments. Plasma-etching parameters are demonstrated to control the resulting nanopillar array morphologies. For MoS_2, these shifted from closely spaced nanocylinders to truncated nanocones, whereas for WS_2 a nanocone profile was always present. A maximum nanopillar height was achieved after complete depletion of the nanosphere masks (approx. 30 s SF_6/C_4F_8 etching): longer etching times led to truncated (MoS2) or amorphous (WS_2) nanostructures. XPS measurements demonstrate that plasma-etching leads to the exposure of 1T metallic sites on WS_2, concurring with previous results obtained for MoS_2 [40]. Electrochemical experiments on freshly-etched samples showed a significant shift in the HER onset potential (≈200 mV for MoS2 and ≈100 mV for WS2). WS_2 enhanced HER activity with respect to MoS2 at equivalent etching conditions was elucidated by Randles–Ševčík and transient chronoamperometry experiments: narrow interspaced nanopillar/truncated nanocone arrays obtained for MoS_2 (interspacing ≤40 nm) did not promote mass transport regimes different from microelectrode array case 4 (i.e. planar macroelectrode). Thus, the HER enhancement observed solely stemmed from the higher exposure of active edge sites. However, the shorter but highly-interspaced WS_2 nanocone arrays presented in some cases significantly higher current densities than those expected for microelectrode array case 4: here the diffusionally independent but inequivalent behaviour of individual naconones in a nanoelectrode array present a high contribution of hemispherical diffusion, neglected in the microelectrode array case. However, the correlation of enhanced HER and electron transfer properties with the aspect ratio of the MoS_2/WS_2 nanocone arrays suggests that the higher exposure of conductive 1T metallic edge sites dictates the HER performance. Finally, morphology stability studies performed on electrochemically-tested, atmosphere exposed plasma-etched WS_2 crystals indicate that minimal surface restructuring upon

electrochemical testing only occurs on high aspect-ratio, closely-interspaced nanocone array structures obtained at long etching times.

Acknowledgments

We thank the EPSRC for financial support via fellowship (REP, EP/L015749/1) and the Centre for Doctoral Training in Fuel Cells and their Fuels (DE-L, NVR, EP/G037116/1). The authors also thank Martin Roe and Nigel Neate from the Nanoscale and Microscale Research Centre (NMRC, EP/L022494/1) for the SEM micrograph acquisition (JEOL 7100F FEG-SEM).

Appendix A. Supplementary data

Supplementary data associated with this article can be found, in the online version, at doi:10.1016/j.apmt.2018.01.006.

References

[1] I. Dincer, C. Acar, Review and evaluation of hydrogen production methods for better sustainability, Int. J. Hydrogen Energy 40 (2014) 11094–11111, http://dx.doi.org/10.1016/j.ijhydene.2014.12.035.
[2] M. Velický, P.S. Toth, From two-dimensional materials to their heterostructures: an electrochemist's perspective, Appl. Mater. Today 8 (2017) 68–103, http://dx.doi.org/10.1016/j.apmt.2017.05.003.
[3] Z. He, W. Que, Molybdenum disulfide nanomaterials: structures, properties, synthesis and recent progress on hydrogen evolution reaction, Appl. Mater. Today 3 (2016) 23–56, http://dx.doi.org/10.1016/j.apmt.2016.02.001.
[4] B. Hinnemann, P. Moses, J. Bonde, K.P. Jørgensen, J.H. Nielsen, S. Horch, et al., Biomimetic hydrogen evolution: MoS_2 nanoparticles as catalyst for hydrogen evolution, J. Am. Chem. Soc. 127 (2005) 5308–5309, http://dx.doi.org/10.1021/ja0504690.
[5] T.F. Jaramillo, K.P. Jørgensen, J. Bonde, J.H. Nielsen, S. Horch, I. Chorkendorff, Identification of active edge sites for electrochemical H_2 evolution from MoS_2 nanocatalysts, Science 317 (2007) 100–103.
[6] H. Huang, L. Chen, C. Liu, X. Liu, S. Fang, W. Liu, et al., Hierarchically Nanostructured MoS_2 with rich in-plane edges as a high-performance electrocatalyst for hydrogen evolution reaction, J. Mater. Chem. A 4 (2016) 14577–14585, http://dx.doi.org/10.1039/C6TA06174E.
[7] Y. Yin, J. Han, Y. Zhang, X. Zhang, P. Xu, Q. Yuan, et al., Contributions of phase, sulfur vacancies, and edges to the hydrogen evolution reaction catalytic activity of porous molybdenum disulfide nanosheets, J. Am. Chem. Soc. 138 (2016) 7965–7972, http://dx.doi.org/10.1021/jacs.6b03714.
[8] J. Xie, H. Zhang, S. Li, R. Wang, X. Sun, M. Zhou, et al., Defect-rich MoS_2 ultrathin nanosheets with additional active edge sites for enhanced electrocatalytic hydrogen evolution, Adv. Mater. 25 (2013) 5807–5813, http://dx.doi.org/10.1002/adma.201302685.
[9] L. Lin, N. Miao, Y. Wen, S. Zhang, P. Ghosez, Z. Sun, et al., Sulfur-depleted monolayered molybdenum disulfide nanocrystals for superelectrochemical hydrogen evolution reaction, ACS Nano 10 (2016) 8929–8937, http://dx.doi.org/10.1021/acsnano.6b04904.
[10] Y. Zhang, L. Zuo, Y. Huang, L. Zhang, F. Lai, W. Fan, et al., In-situ growth of few-layered MoS_2 nanosheets on highly porous carbon aerogel as advanced electrocatalysts for hydrogen evolution reaction, ACS Sustain. Chem. Eng. 3 (2015) 3140–3148, http://dx.doi.org/10.1021/acssuschemeng.5b00700.
[11] K.C. Pham, Y.H. Chang, D.S. McPhail, C. Mattevi, A.T.S. Wee, D.H.C. Chua, Amorphous molybdenum sulfide on graphene-carbon nanotube hybrids as highly active hydrogen evolution reaction catalysts, ACS Appl. Mater. Interfaces 8 (2016) 5961–5971, http://dx.doi.org/10.1021/acsami.5b09690.
[12] D. McAteer, Z. Gholamvand, N. McEvoy, A. Harvey, E. O'Malley, G.S. Duesberg, et al., Thickness dependence and percolation scaling of hydrogen production rate in MoS_2 nanosheet and nanosheet–carbon nanotube composite catalytic electrodes, ACS Nano 10 (2016) 672–683, http://dx.doi.org/10.1021/acsnano.5b05907.
[13] D. Escalera-López, Y. Niu, J. Yin, K. Cooke, N.V. Rees, R.E. Palmer, Enhancement of the hydrogen evolution reaction from Ni-MoS_2 hybrid nanoclusters, ACS Catal. (2016) 6008–6017, http://dx.doi.org/10.1021/acscatal.6b01274.
[14] D. Merki, H. Vrubel, L. Rovelli, S. Fierro, X. Hu, Fe, Co, and Ni ions promote the catalytic activity of amorphous molybdenum sulfide films for hydrogen evolution, Chem. Sci. 3 (2012) 2515, http://dx.doi.org/10.1039/c2sc20539d.
[15] H. Wang, C. Tsai, D. Kong, K. Chan, F. Abild-Pedersen, J.K. Nørskov, et al., Transition-metal doped edge sites in vertically aligned MoS_2 catalysts for enhanced hydrogen evolution, Nano Res. 8 (2015) 566–575, http://dx.doi.org/10.1007/s12274-014-0677-7.
[16] L. Yu, B.Y. Xia, X. Wang, X.W. Lou, General formation of M-MoS_3 (M = Co, Ni) hollow structures with enhanced electrocatalytic activity for hydrogen evolution, Adv. Mater. 28 (2016) 92–97, http://dx.doi.org/10.1002/adma.201504024.
[17] J. Deng, H. Li, J. Xiao, Y. Tu, D. Deng, H. Yang, et al., Triggering the electrocatalytic hydrogen evolution activity of the inert two-dimensional MoS_2 surface via single-atom metal doping, Energy Environ. Sci. 8 (2015) 1594–1601, http://dx.doi.org/10.1039/C5EE00751H.
[18] K. Qi, S. Yu, Q. Wang, W. Zhang, J. Fan, W.T. Zheng, et al., Decoration of the inert basal plane of defect-rich MoS_2 with Pd atoms for achieving Pt-similar HER activity, J. Mater. Chem. A 4 (2016) 4025–4031, http://dx.doi.org/10.1039/C5TA10337A.
[19] M.K. Dawood, T.H. Liew, P. Lianto, M.H. Hong, S. Tripathy, J.T.L. Thong, et al., Interference lithographically defined and catalytically etched, large-area silicon nanocones from nanowires, Nanotechnology 21 (2010) 205305, http://dx.doi.org/10.1088/0957-4484/21/20/205305.
[20] M.C. Henstridge, R.G. Compton, Mass transport to micro- and nanoelectrodes and their arrays: a review, Chem. Rec. 12 (2012) 63–71, http://dx.doi.org/10.1002/tcr.201100032.
[21] Y. Liu, A. Holzinger, P. Knittel, L. Poltorak, A. Gamero-Quijano, W.D.A. Rickard, et al., Visualization of diffusion within nanoarrays, Anal. Chem. 88 (2016) 6689–6695, http://dx.doi.org/10.1021/acs.analchem.6b00513.
[22] D.W.M. Arrigan, Nanoelectrodes, nanoelectrode arrays and their applications, Analyst 129 (2004) 1157–1165, http://dx.doi.org/10.1039/b415395m.
[23] S.P. Branagan, N.M. Contento, P.W. Bohn, Enhanced mass transport of electroactive species to annular nanoband electrodes embedded in nanocapillary array membranes, J. Am. Chem. Soc. 134 (2012) 8617–8624, http://dx.doi.org/10.1021/ja3017158.
[24] Y. Qiu, S.-F. Leung, Q. Zhang, B. Hua, Q. Lin, Z. Wei, et al., Efficient photoelectrochemical water splitting with ultrathin fi lms of hematite on three-dimensional nanophotonic structures, Nano Lett. 14 (2014) 2123–2129.
[25] K.X. Wang, Z. Yu, V. Liu, M.L. Brongersma, T.F. Jaramillo, S. Fan, Nearly total solar absorption in ultrathin nanostructured iron oxide for efficient photoelectrochemical water splitting, ACS Photonics 1 (2014) 235–240, http://dx.doi.org/10.1021/ph4001026.
[26] R. Ge, H. Du, K. Tao, Q. Zhang, L. Chen, Cobalt-borate nanoarray: an efficient and durable electrocatalyst for water oxidation under benign conditions, ACS Appl. Mater. Interfaces 9 (2017) 15383–15387, http://dx.doi.org/10.1021/acsami.7b00184.
[27] L. Yang, L. Xie, R. Ge, R. Kong, Z. Liu, G. Du, et al., Core–shell NiFe-LDH@NiFe-Bi nanoarray: in situ electrochemical surface derivation preparation toward efficient water oxidation electrocatalysis in near-neutral media, ACS Appl. Mater. Interfaces 9 (2017) 19502–19506, http://dx.doi.org/10.1021/acsami.7b01637.
[28] Z. Fan, R. Kapadia, P.W. Leu, X. Zhang, Y.L. Chueh, K. Takei, et al., Ordered arrays of dual-diameter nanopillars for maximized optical absorption, Nano Lett. 10 (2010) 3823–3827, http://dx.doi.org/10.1021/nl1010788.
[29] J. Zhu, Z. Yu, G.F. Burkhard, C.-M. Hsu, S.T. Connor, Y. Xu, et al., Optical absorption enhancement in amorphous silicon nanowire and nanocone arrays, Nano Lett. 9 (2009) 279–282, http://dx.doi.org/10.1021/nl802886y.
[30] Y. Qiu, Y. Zhao, X. Yang, W. Li, Z. Wei, J. Xiao, et al., Three-dimensional metal/oxide nanocone arrays for high-performance electrochemical pseudocapacitors, Nanoscale 6 (2014) 3626–3631, http://dx.doi.org/10.1039/c3nr06675d.
[31] L. Cui, L. Huang, M. Ji, Y. Wang, H. Shi, Y. Zuo, et al., High-performance $MgCo_2O_4$ nanocone arrays grown on three-dimensional nickel foams: preparation and application as binder-free electrode for pseudo-supercapacitor, J. Power Sources 333 (2016) 118–124, http://dx.doi.org/10.1016/j.jpowsour.2016.09.159.
[32] B.K. You, J.M. Kim, D.J. Joe, K. Yang, Y. Shin, Y.S. Jung, et al., Reliable memristive switching memory devices enabled by densely packed silver nanocone arrays as electric-field concentrators, ACS Nano 10 (2016) 9478–9488, http://dx.doi.org/10.1021/acsnano.6b04578.
[33] N. Wang, T. Hang, H. Ling, A. Hu, M. Li, High-performance Si-based 3D Cu nanostructured electrode assembly for rechargeable lithium batteries, J. Mater. Chem. A 3 (2015) 11912–11919, http://dx.doi.org/10.1039/C5TA01978H.
[34] X. Wang, Z. Yang, X. Sun, X. Li, D. Wang, P. Wang, et al., NiO nanocone array electrode with high capacity and rate capability for Li-ion batteries, J. Mater. Chem. 21 (2011) 9988, http://dx.doi.org/10.1039/c1jm11490e.
[35] J. Guo, Y. Cai, S. Zhang, S. Chen, F. Zhang, Core–shell structured o-$LiMnO_2$@Li_2CO_3 nanosheet array cathode for high-performance, wide-temperature-tolerance lithium-ion batteries, ACS Appl. Mater. Interfaces 8 (2016) 16116–16124, http://dx.doi.org/10.1021/acsami.6b04616.
[36] M. Ongaro, P. Ugo, Bioelectroanalysis with nanoelectrode ensembles and arrays, Anal. Bioanal. Chem. 405 (2013) 3715–3729, http://dx.doi.org/10.1007/s00216-012-6552-z.
[37] V. Anandan, X. Yang, E. Kim, Y.L. Rao, G. Zhang, Role of reaction kinetics and mass transport in glucose sensing with nanopillar array electrodes, J. Biol. Eng. 1 (2007) 5, http://dx.doi.org/10.1186/1754-1611-1-5.
[38] S. Daniele, E. De Faveri, I. Kleps, A. Angelescu, Voltammetric characterization of micro- and submicrometer-electrode arrays of conical shape for electroanalytical use, Electroanalysis 18 (2006) 1749–1756, http://dx.doi.org/10.1002/elan.200603595.
[39] L. Qiu, W. Wang, A. Zhang, N. Zhang, T. Lemma, H. Ge, et al., Core–shell nanorod columnar array combined with gold nanoplate-nanosphere assemblies enable powerful in situ SERS detection of bacteria, ACS Appl. Mater. Interfaces 8 (2016) 24394–24403, http://dx.doi.org/10.1021/acsami.6b06674.

[40] H.A. Burch, M. Isaacs, K. Wilson, R.E. Palmer, N.V. Rees, Electrocatalytic regeneration of atmospherically aged MoS_2 nanostructures via solution-phase sulfidation, RSC Adv. 6 (2016) 26689–26695, http://dx.doi.org/10.1039/C6RA03326A.
[41] D. Escalera-López, R. Griffin, M. Isaacs, K. Wilson, R.E. Palmer, N.V. Rees, Electrochemical sulfidation of WS_2 nanoarrays: strong dependence of hydrogen evolution activity on transition metal sulfide surface composition, Electrochem. Commun. 81 (2017) 106–111, http://dx.doi.org/10.1016/j.elecom.2017.06.016.
[42] K. Seeger, R.E. Palmer, Fabrication of ordered arrays of silicon nanopillars in silicon pillars, J. Phys. D: Appl. Phys. 32 (1999) L129–L132, http://dx.doi.org/10.1088/0022-3727/32/24/102.
[43] K. Seeger, R.E. Palmer, Fabrication of silicon cones and pillars using rough metal films as plasma etching masks, Appl. Phys. Lett. 74 (1999) 1627–1629, http://dx.doi.org/10.1063/1.123638.
[44] A. Wellner, P.R. Preece, J.C. Fowler, R.E. Palmer, Fabrication of ordered arrays of silicon nanopillars in silicon-on-insulator wafers, Microelectron. Eng. 5758 (2001) 919–924, http://dx.doi.org/10.1088/0022-3727/32/24/102.
[45] R.S. Nicholson, Theory and application of cyclic voltammetry for measurement of electrode reaction kinetics, Anal. Chem. 37 (1965) 1351–1355, http://dx.doi.org/10.1021/ac60230a016.
[46] R.J. Klinger, J.K. Kochi, Electron-transfer kinetics from cyclic voltammetry. Quantitative description of electrochemical reversibility, J. Phys. Chem. 85 (1981) 1731–1741, http://dx.doi.org/10.1021/j150612a028.
[47] S.J. Konopka, B. McDuffie, Diffusion coefficients of ferri- and ferrocyanide ions in aqueous media, using twin-electrode thin-layer electrochemistry, Anal. Chem. 42 (1970) 1741–1746, http://dx.doi.org/10.1021/ac50160a042.
[48] A.J. Bard, L.R. Faulkner, Electrochemical Methods: Fundamentals and Applications, 2nd ed., John Wiley and Sons Ltd, New York, 2001, http://dx.doi.org/10.1016/B978-0-12-381373-2.00056-9.
[49] M.I. Petrescu, Theoretical hardness calculated from crystallo-chemical data for MoS_2 and WS_2 crystals and nanostructures, Acta Crystallogr. Sect. B: Struct. Sci. 68 (2012) 501–510, http://dx.doi.org/10.1107/S0108768112033149.
[50] A.P. Shpak, A.M. Korduban, L.M. Kulikov, T.V. Kryshchuk, N.B. Konig, V.O. Kandyba, XPS studies of the surface of nanocrystalline tungsten disulfide, J. Electron Spectros. Relat. Phenomena 181 (2010) 234–238, http://dx.doi.org/10.1016/j.elspec.2010.05.030.
[51] A. Ambrosi, Z. Sofer, M. Pumera, 2H → 1T phase transition and hydrogen evolution activity of MoS2, $MoSe_2$, WS_2 and WSe_2 strongly depends on the MX2 composition, Chem. Commun. 51 (2015) 8450–8453, http://dx.doi.org/10.1039/c5cc00803d.
[52] K.M. McCreary, A.T. Hanbicki, G.G. Jernigan, J.C. Culbertson, B.T. Jonker, Synthesis of large-area WS_2 monolayers with exceptional photoluminescence, Sci. Rep. 6 (2016) 19159, http://dx.doi.org/10.1038/srep19159.
[53] A. Katrib, F. Hemming, P. Wehrer, L. Hilaire, G. Maire, The multi-surface structure and catalytic properties of partially reduced WO_3, WO_2 and WC + O_2 or W + O_2 as characterized by XPS, J. Electron Spectros. Relat. Phenomena 76 (1995) 195–200, http://dx.doi.org/10.1016/0368-2048(95)02451-4.
[54] A.A. Audi, P.M.A. Sherwood, X-ray photoelectron spectroscopic studies of sulfates and bisulfates interpreted by Xa and band structure calculations, Surf. Interface Anal. 29 (2000) 265–275, http://dx.doi.org/10.1002/sia.1211.
[55] M.Y. Smirnov, A.V. Kalinkin, A.V. Pashis, A.M. Sorokin, A.S. Noskov, K.C. Kharas, et al., Interaction of Al_2O_3 and CeO_2 surfaces with SO_2 and SO_2 + O_2 studied by X-ray photoelectron spectroscopy, J. Phys. Chem. B 109 (2005) 11712–11719, http://dx.doi.org/10.1021/jp0508249.
[56] S. Kim, M.S. Choi, D. Qu, C.H. Ra, X. Liu, M. Kim, et al., Effects of plasma treatment on surface properties of ultrathin layered MoS_2, 2D Mater. 3 (2016) 035002, http://dx.doi.org/10.1088/2053-1583/3/3/035002.
[57] S. Xiao, P. Xiao, X. Zhang, D. Yan, X. Gu, F. Qin, et al., Atomic-layer soft plasma etching of MoS_2, Sci. Rep. 6 (2016) 1–8, http://dx.doi.org/10.1038/srep19945.
[58] N. Choudhary, M.R. Islam, N. Kang, L. Tetard, Y. Jung, S.I. Khondaker, Two-dimensional lateral heterojunction through bandgap engineering of MoS_2 via oxygen plasma, J. Phys. Condens. Matter 28 (2016), http://dx.doi.org/10.1088/0953-8984/28/36/364002.
[59] N.M.D. Brown, N. Cui, A. Mckinley, An XPS study of the surface modification of natural MoS 2 following treatment in an RF-oxygen plasma, Appl. Surf. Sci. 134 (1998) 11–21.
[60] J. Hong, Z. Hu, M. Probert, K. Li, D. Lv, X. Yang, et al., Exploring atomic defects in molybdenum disulphide monolayers, Nat. Commun. 6 (2015) 1–8, http://dx.doi.org/10.1038/ncomms7293.
[61] R. Prehn, L. Abad, D. Sánchez-Molas, M. Duch, N. Sabaté, F.J. Del Campo, et al., Microfabrication and characterization of cylinder micropillar array electrodes, J. Electroanal. Chem. 662 (2011) 361–370, http://dx.doi.org/10.1016/j.jelechem.2011.09.002.
[62] D. Sánchez-Molas, J.P. Esquivel, N. Sabaté, F.X. Muñoz, F.J. del Campo, High aspect-ratio, fully conducting gold micropillar array electrodes: silicon micromachining and electrochemical characterization, J. Phys. Chem. C 116 (2012) 18831–18846, http://dx.doi.org/10.1021/jp305339k.
[63] D. Menshykau, X.-J. Huang, N.V. Rees, F.J. del Campo, F.X. Muñoz, R.G. Compton, Investigating the concept of diffusional independence. Potential step transients at nano- and micro-electrode arrays: theory and experiment, Analyst 134 (2009) 343–348, http://dx.doi.org/10.1039/b816223a.
[64] T.J. Davies, R.G. Compton, The cyclic and linear sweep voltammetry of regular and random arrays of microdisc electrodes: theory, J. Electroanal. Chem. 585 (2005) 63–82, http://dx.doi.org/10.1016/j.jelechem.2005.07.022.
[65] C. Amatore, J.M. Savéant, D. Tessier, Charge transfer at partially blocked surfaces – a model for the case of microscopic active and inactive sites, J. Electroanal. Chem. 147 (1983) 39–51, http://dx.doi.org/10.1016/S0022-0728(83)80055-2.
[66] N. Godino, X. Borrise, F.X. Muñoz, F.J. Del Campo, R.G. Compton, Mass transport to nanoelectrode arrays and limitations of the diffusion domain approach: theory and experiment, J. Phys. Chem. C 113 (2009) 11119–11125, http://dx.doi.org/10.1021/jp9031354.
[67] A.S. Peinetti, R.S. Gilardoni, M. Mizrahi, F.G. Requejo, G.A. González, F. Battaglini, Numerical simulation of the diffusion processes in nanoelectrode arrays using an axial neighbor symmetry approximation, Anal. Chem. 88 (2016) 5752–5759, http://dx.doi.org/10.1021/acs.analchem.6b00039.
[68] E.J.F. Dickinson, I. Streeter, R.G. Compton, Chronoamperometry and cyclic voltammetry at conical electrodes, microelectrodes, and electrode arrays: theory, J. Phys. Chem. B 112 (2008) 4059–4066, http://dx.doi.org/10.1021/jp711936y.
[69] T. Shinagawa, A.T. Garcia-Esparza, K. Takanabe, Insight on Tafel slopes from a microkinetic analysis of aqueous electrocatalysis for energy conversion, Sci. Rep. 5 (2015) 13801, http://dx.doi.org/10.1038/srep13801.
[70] D. Voiry, M. Salehi, R. Silva, T. Fujita, M. Chen, Conducting MoS_2 nanosheets as catalysts for hydrogen evolution reaction, Nano Lett. 13 (2013) 6222–6227, http://pubs.acs.org/doi/abs/10.1021/nl403661s (accessed 15.12.15).
[71] D. Voiry, H. Yamaguchi, J. Li, R. Silva, D.C.B. Alves, T. Fujita, et al., Enhanced catalytic activity in strained chemically exfoliated WS_2 nanosheets for hydrogen evolution, Nat. Mater. 12 (2013) 850–855, http://dx.doi.org/10.1038/nmat3700.
[72] M.-R. Gao, M.K.Y. Chan, Y. Sun, Edge-terminated molybdenum disulfide with a 9.4-Å interlayer spacing for electrochemical hydrogen production, Nat. Commun. 6 (2015) 7493, http://dx.doi.org/10.1038/ncomms8493.
[73] B.E. Conway, B.V. Tilak, Interfacial processes involving electrocatalytic evolution and oxidation of H_2, and the role of chemisorbed H, Electrochim. Acta 47 (2002) 3571–3594.
[74] A.Y.S. Eng, A. Ambrosi, Z. Sofer, P. Simek, M. Pumera, Electrochemistry of transition metal dichalcogenides: strong dependence on the metal-to-chalcogen composition and exfoliation method, ACS Nano 8 (2014) 12185–12198.
[75] X. Chia, A. Ambrosi, Z. Sofer, J. Luxa, M. Pumera, Catalytic and charge transfer properties of transition metal dichalcogenides arising from electrochemical pretreatment, ACS Nano 9 (2015) 5164–5179.
[76] M. Velický, M.A. Bissett, P.S. Toth, H.V. Patten, S.D. Worrall, A.N.J. Rodgers, et al., Electron transfer kinetics on natural crystals of MoS_2 and graphite, Phys. Chem. Chem. Phys. 17 (2015) 17844–17853, http://dx.doi.org/10.1039/C5CP02490K.
[77] M. Velický, M.A. Bissett, C.R. Woods, P.S. Toth, T. Georgiou, I.A. Kinloch, et al., Photoelectrochemistry of pristine mono- and few-layer MoS_2, Nano Lett. 16 (2016) 2023–2032, http://dx.doi.org/10.1021/acs.nanolett.5b05317.
[78] H. Li, M. Du, M.J. Mleczko, A.L. Koh, Y. Nishi, E. Pop, et al., Kinetic study of hydrogen evolution reaction over strained MoS_2 with sulfur vacancies using scanning electrochemical microscopy, J. Am. Chem. Soc. 138 (2016) 5123–5129, http://dx.doi.org/10.1021/jacs.6b01377.
[79] E. Parzinger, E. Mitterreiter, M. Stelzer, F. Kreupl, J.W. Ager, A.W. Holleitner, et al., Hydrogen evolution activity of individual mono-, bi-, and few-layer MoS_2 towards photocatalysis, Appl. Mater. Today 8 (2017) 132–140, http://dx.doi.org/10.1016/j.apmt.2017.04.007.
[80] N. Mohamad Latiff, L. Wang, C.C. Mayorga-Martinez, Z. Sofer, A.C. Fisher, M. Pumera, Valence and oxide impurities in MoS_2 and WS_2 dramatically change their electrocatalytic activity towards proton reduction, Nanoscale 8 (2016) 16752–16760, http://dx.doi.org/10.1039/C6NR03086F.
[81] J. Xie, J. Zhang, S. Li, F. Grote, X. Zhang, H. Zhang, et al., Controllable disorder engineering in oxygen-incorporated MoS_2 ultrathin nanosheets for efficient hydrogen evolution, J. Am. Chem. Soc. 135 (2013) 17881–17888, http://dx.doi.org/10.1021/ja408329q.
[82] L.R.L. Ting, Y. Deng, L. Ma, Y.J. Zhang, A.A. Peterson, B.S. Yeo, Catalytic activities of sulfur atoms in amorphous molybdenum sulfide for the electrochemical hydrogen evolution reaction, ACS Catal. 6 (2016) 861–867, http://dx.doi.org/10.1021/acscatal.5b02369.